Moiré engineering of electronic phenomena in correlated oxides

Xinzhong Chen[1,8], Xiaodong Fan[2,8], Lin Li[2,8 ✉], Nan Zhang[2], Zhijing Niu[1], Tengfei Guo[3], Suheng Xu[1], Han Xu[2,4], Dongli Wang[2], Huayang Zhang[2], A. S. McLeod[5], Zhenlin Luo[4], Qingyou Lu[2,3], Andrew J. Millis[5,6], D. N. Basov[5 ✉], Mengkun Liu[1,7 ✉] and Changgan Zeng[2 ✉]

Moiré engineering has recently emerged as an effective approach to control quantum phenomena in condensed matter systems[1–6]. In van der Waals heterostructures, moiré patterns can be formed by lattice misorientation between adjacent atomic layers, creating long-range electronic order. Moiré engineering has so far been executed solely in stacked van der Waals multilayers. Here we describe electronic moiré patterns in films of a prototypical magnetoresistive oxide, La$_{0.67}$Sr$_{0.33}$MnO$_3$, epitaxially grown on LaAlO$_3$ substrates. Using scanning probe nanoimaging, we observe microscopic moiré profiles attributed to the coexistence and interaction of two distinct incommensurate patterns of strain modulation within these films. The net effect is that both the electronic conductivity and ferromagnetism of La$_{0.67}$Sr$_{0.33}$MnO$_3$ are modulated by periodic moiré textures extending over mesoscopic scales. Our work provides a potential route to achieving spatially patterned electronic textures on demand in strained epitaxial materials.

Moiré patterns emerge from overlaying two sets of mildly dissimilar periodic motifs. In two-dimensional van der Waals systems, moiré patterns have been achieved by stacking two-dimensional atomic layers with slightly incommensurate periodicities and/or small twist angles[7]. Fascinating properties have emerged in two-dimensional moiré systems, including superconductivity and Mott insulating states in magic-angle graphene superlattices[1,2], moiré excitons in transition metal dichalcogenide heterobilayers[3–5] and topological conducting channels in twisted bilayer graphene[6]. However, moiré-type electronic modulations have never been experimentally demonstrated or theoretically proposed in correlated transition metal oxides (CTMOs), which are known to host rich interactions between charge, spin, lattice and orbital degrees of freedom[8,9]. Herein, we demonstrate that moiré engineering is applicable beyond van der Waals materials and report mesoscale spatial moiré modulations of coupled conductivity and ferromagnetism in strained thin films of a correlated oxide.

A universal property of CTMOs is the competition and coexistence of multiple order parameters that spontaneously give rise to spatially textured physical properties[10]. These emergent electronic textures are particularly prominent in manganites, including La$_{1-x}$Ca$_x$MnO$_3$ and related materials[11–14]. However, deterministic

creation of spatially ordered patterns remains a daunting task. Here, we utilize interactions between two distinct sources of periodic strain modulation in epitaxial La$_{0.67}$Sr$_{0.33}$MnO$_3$ (LSMO) films grown on LaAlO$_3$ (LAO) substrates. When these two modulations are collocated in real space, they coproduce moiré-like energy landscapes that locally modulate conductivity and ferromagnetism.

We investigated 20-nm-thick LSMO films on LAO substrates (see Methods for details). The high crystalline and epitaxial quality is confirmed by a combination of X-ray diffraction (XRD) and cross-sectional transmission electron microscopy (TEM) (Extended Data Fig. 1). Temperature-dependent resistivity and magnetic moment reveal a characteristic second-order phase transition from ferromagnetic metal to paramagnetic metal at $T_C \sim 340$ K (Fig. 1a). This T_C is reduced compared with the bulk value ($\sim$370 K; ref. [15]), attesting to the large in-plane compressive strain imposed by the substrate[16]. We harnessed epitaxial control to define the local compressive strain patterns ultimately giving rise to moiré textures. First, we note that LSMO films on LAO possess highly oriented rhombohedral twin domains[17–21] that stem from local relaxations of substrate-imposed shear strain (see Fig. 1b, Extended Data Fig. 3 and Supplementary Note 2). As schematically shown in Fig. 1c, such a periodic structure results in a striped strain modulation[18,21], which we designate as domain stripes (DSs). On the other hand, surface miscut steps in the LAO substrate (see Fig. 1d,e and Extended Data Fig. 4) serve as another source of periodically modulated strain in LSMO. The resultant periodic strain modulation in LSMO, which we name miscut stripes (MSs), does not necessarily align with any specific crystal axis but depends strictly on the local miscut surface of the substrate[22] (see Supplementary Note 3). The spatial coexistence of DS and MS modulations yields moiré landscapes with domain sizes governed by the periodicities and relative angles of the two constituent stripe motifs (Fig. 1f).

Nano-optical imaging provides direct evidence for the promise and possibility of moiré strain engineering. We utilized infrared scattering-type scanning near-field optical microscopy (s-SNOM) to visualize nanoscale moiré phenomena in strained LSMO/LAO (see Methods for details). The amplitude of the nano-infrared signal demodulated at the second harmonic of the tip tapping frequency (S_2) provides a local probe of the optical conductivity with ~25-nm

[1]Department of Physics and Astronomy, Stony Brook University, Stony Brook, NY, USA. [2]International Center for Quantum Design of Functional Materials, Hefei National Laboratory for Physical Sciences at the Microscale, CAS Key Laboratory of Strongly Coupled Quantum Matter Physics, Department of Physics, and Synergetic Innovation Center of Quantum Information & Quantum Physics, University of Science and Technology of China, Hefei, Anhui, China. [3]Anhui Province Key Laboratory of Condensed Matter Physics at Extreme Conditions, High Magnetic Field Laboratory of the Chinese Academy of Sciences, Hefei, Anhui, China. [4]National Synchrotron Radiation Laboratory & CAS Key Laboratory of Materials for Energy Conversion, University of Science and Technology of China, Hefei, Anhui, China. [5]Department of Physics, Columbia University, New York, NY, USA. [6]Center for Computational Quantum Physics, The Flatiron Institute, New York, NY, USA. [7]National Synchrotron Light Source II, Brookhaven National Laboratory, Upton, NY, USA. [8]These authors contributed equally: Xinzhong Chen, Xiaodong Fan, Lin Li. ✉e-mail: lilin@ustc.edu.cn; db3056@columbia.edu; mengkun.liu@stonybrook.edu; cgzeng@ustc.edu.cn
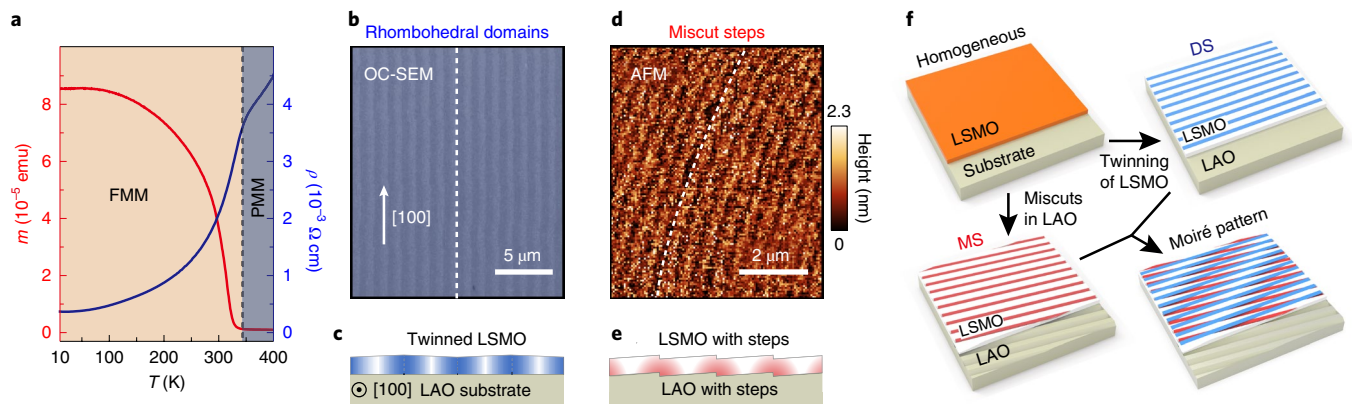
Fig. 1 | Two types of periodic strain modulation in LSMO thin films. a, Temperature-dependent resistivity ρ and magnetic moment m of an LSMO thin film under study. The magnetic moment was measured at 100 Oe on warming after cooling the sample in a 100-Oe field. The black dashed line indicates T_C. FMM, ferromagnetic metal; PMM, paramagnetic metal. **b**, Orientation-contrast scanning electron micrograph (OC-SEM) image of an LSMO thin film, showing surface rhombohedral domains with a width of ~590 nm aligned along the [100] direction. **c**, Schematic of the rhombohedral-domain-induced strain modulation in an LSMO–LAO cross-section. **d**, AFM image of an LSMO thin film, showing topographic surface changes due to crystal miscut steps in the LAO substrate. The period is ~500 nm. White dashed lines in **b** and **d** indicate the directions of the rhombohedral domains and miscut steps, respectively. **e**, Schematic of the miscut-step-induced strain modulation in an LSMO–LAO cross-section. **f**, Schematic demonstration of how the spatial coexistence of DSs and MSs yields the combined moiré patterns comprising regions of local commensuration and incommensuration.
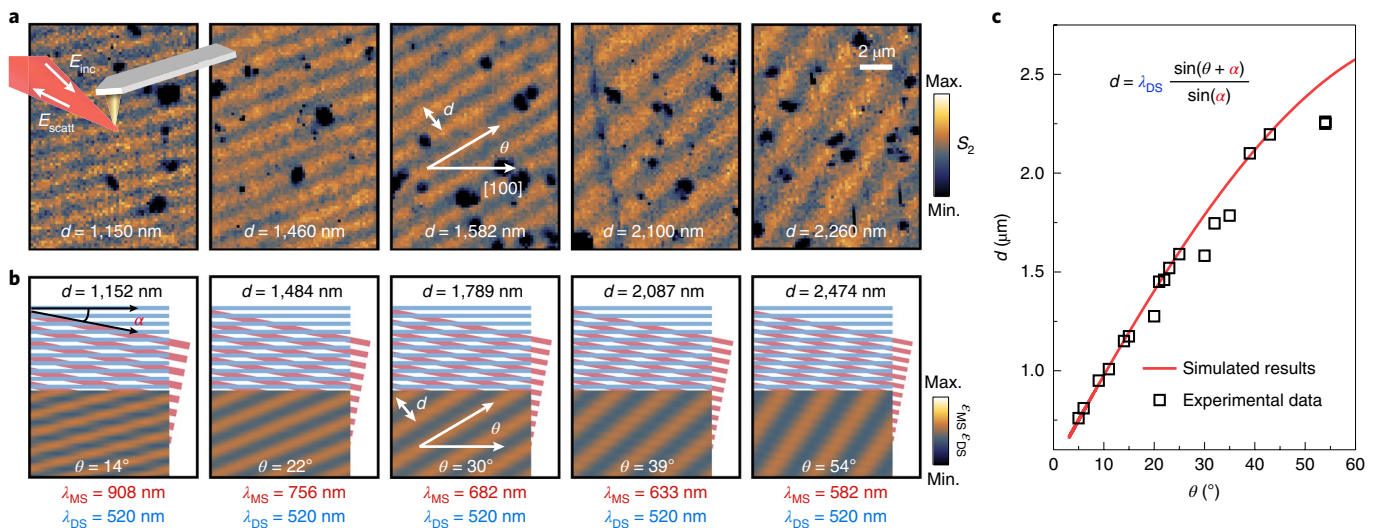

Fig. 2 | Electronic moiré patterns in LSMO films. a, Nano-infrared maps of S_2 obtained at the infrared wavelength of 10.7 μm and collected in different regions of a representative LSMO/LAO film. **b**, Top: simulations of the moiré patterns formed by superimposing two periodic striped motifs. Blue, DSs; red, MSs. From left to right, the λ_{MS} are 908 nm, 756 nm, 682 nm, 633 nm and 582 nm, respectively, while λ_{DS} and the twist angle between DSs and MSs are fixed at 520 nm and 11°, respectively. Bottom: simulations generated by multiplying the two striped patterns using the same parameters as in the top half. **c**, The moiré pattern periodicity as a function of θ.

spatial resolution[23,24]. In Fig. 2a, we display maps of the two-dimensional nano-infrared contrast, revealing periodic modulations of the local electronic response in LSMO/LAO. Notably, the periodicity d is revealed to be considerably larger than that of either the DSs or MSs. Moreover, d appears to be governed by the orientation of these patterns with respect to the [100] direction of the LAO substrate (also see Extended Data Fig. 5). These systematic trends point to a unified underlying mechanism for the formation of electronic patterns that we link to the emergent moiré pattern of combined periodic strains.

We now proceed to elucidate the rich real-space structures of conductivity observed in our strained films. We first note that the two sets of overlaid unidirectional stripes with relatively small spacings readily produce longer-period textures (top panels in

Fig. 2b). Microscopic strain fields $\boldsymbol{\varepsilon}_{DS}$ and $\boldsymbol{\varepsilon}_{MS}$ that vary sinusoidally in space present a realistic scenario for our films. Here we associate $\boldsymbol{\varepsilon}_{DS}$ with the DSs and $\boldsymbol{\varepsilon}_{MS}$ with the MSs introduced in Fig. 1. As demonstrated in the bottom panels of Fig. 2b, we were able to reproduce the key trends in the images in Fig. 2a by assuming that the observed textures are a direct manifestation of the product $\boldsymbol{\varepsilon}_{DS} \cdot \boldsymbol{\varepsilon}_{MS}$ of these two sinusoidal strain fields. This product term naturally stems from the nonlinear relationship between the strain and the conductivity, which originates in the strain-induced nonlinear T_C modulation in LSMO[16,25–27] (detailed in Supplementary Note 4). Our experimental result attests to the large magnitude of nonlinear coefficient for the cross-term $\boldsymbol{\varepsilon}_{DS} \cdot \boldsymbol{\varepsilon}_{MS}$, which originates from the cubic (O_h) point symmetry of Mn in the cubic perovskite structure
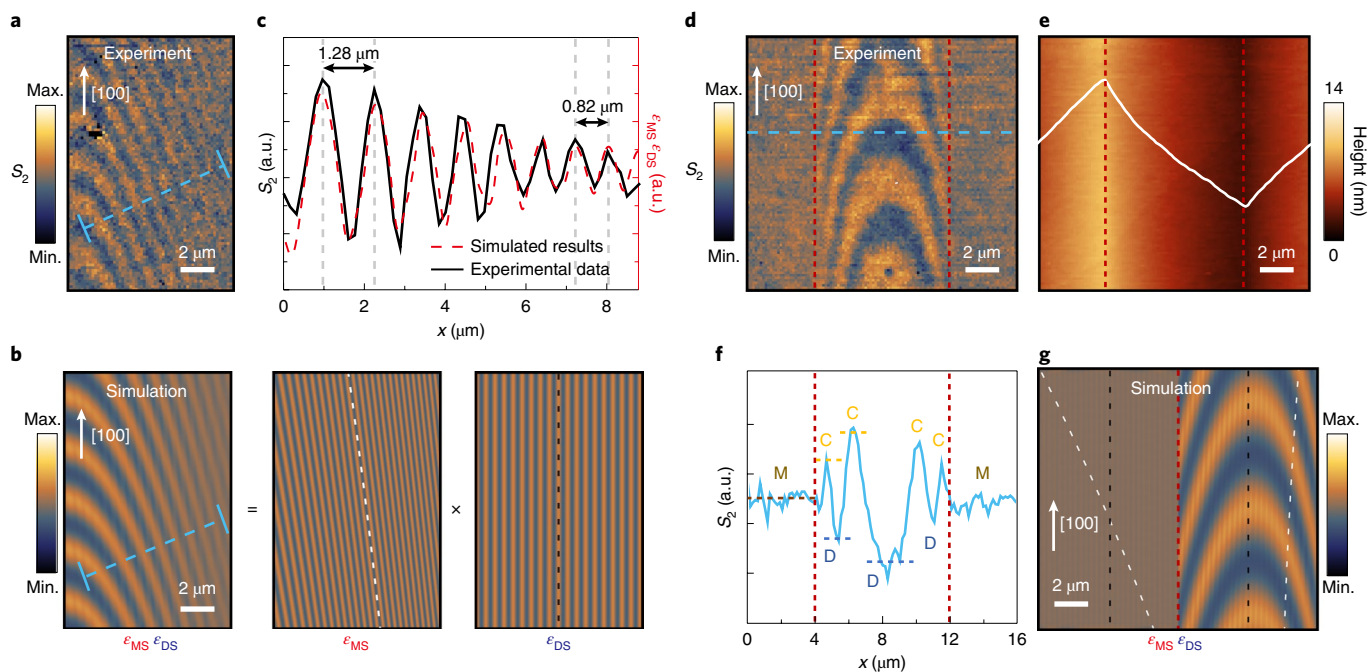
Fig. 3 | Curved electronic moiré patterns in LSMO films. a,b, Infrared near-field image of a curved moiré pattern (**a**) and the corresponding simulation (**b**). The simulation is generated by multiplying two periodic striped patterns representing MSs and DSs. The white and black dashed lines in **b** indicate the MS and DS orientations, respectively. **c,** Line profiles from the blue dashed lines in **a** and **b**, exhibiting high consistency between the experimental and the simulated contrast. a.u., arbitrary units. **d,e,** Infrared near-field image and corresponding AFM image, respectively, showing alternating moiré and non-moiré regions across the LAO twin boundaries (indicated by red dashed lines). The white solid line in **e** is the AFM height profile. **f,** Line profile of the nano-infrared contrast along the blue dashed line in **d**. The different signal levels are marked 'C', 'D' and 'M', which represent constructively strained, destructively strained and mixed strained regions, respectively. **g,** Simulation of the image in **d** with the moiré pattern only visible on the right-hand side. Note that the MSs (orientation indicated by white dashed lines) change orientation across the LAO twin boundary (red dashed line), while the DSs (orientation indicated by black dashed lines) are consistently along the LAO [100] direction. The simulation details are shown in Extended Data Fig. 8c.

as well as the large Jahn–Teller effect due to strong electron–lattice coupling in LSMO[25]. We note that, in our simulated image, a local Gaussian average filter with radius ~100 nm is applied to account for the finite spatial resolution of the near-field probe and possible local strain relaxation (Extended Data Fig. 6).

The concurrent evolution of the moiré fringe d and angle θ (defined as the angle between the orientation of fringes and the LAO [100] direction) can be theoretically obtained by multiplying two sinusoidal waves with wavevectors $\mathbf{k}_{DS} = \left(0, \frac{2\pi}{\lambda_{DS}}\right)$ and $\mathbf{k}_{MS} = \left(\frac{2\pi \sin(\alpha)}{\lambda_{MS}}, \frac{2\pi \cos(\alpha)}{\lambda_{MS}}\right)$, where λ_{DS} and λ_{MS} are the DS and MS periodicities, respectively, and α is the twist angle between the DSs and MSs. The resultant moiré pattern yields $\theta = \text{arccot}\left(\frac{\lambda_{MS} - \lambda_{DS} \cos(\alpha)}{\lambda_{DS} \sin(\alpha)}\right)$ and $d = \frac{2\pi}{|\mathbf{k}_{DS} - \mathbf{k}_{MS}|} = \frac{\lambda_{DS} \sin(\theta + \alpha)}{\sin(\alpha)}$. We found that the d–θ relation shown in Fig. 2a and Extended Data Fig. 5 can be reproduced by solely adjusting the λ_{MS}, whose gradual change is expected across the 1×1 mm^2 film due to a long-range variation in the surface miscut angle of the substrate and consequently in the MS periodicity. As shown in Fig. 2b,c, we found excellent agreement between experimental images and theory by monotonically varying λ_{MS} from 908 nm to 582 nm while keeping λ_{DS} and α constant. This agreement verifies that the spatial modulations in optical conductivity observed in the LSMO/LAO samples do indeed arise from the synergistic effect of DSs and MSs. We note that similar moiré fringes were not found in the surface topography of LSMO core-corded with the near-field imaging using atomic force microscopy (AFM), which suggests that the strong nonlinear coupling of optical conductivity to the local strain is an essential ingredient for deterministic occurrence of observed moiré patterns.

Apart from the unidirectional moiré fringes in Fig. 2, more complex moiré patterns can be obtained (Extended Data Fig. 7). For example, we observed curved moiré fringes in another LSMO/LAO sample of the same ~20-nm thickness (Fig. 3a). In Fig. 3b we show that such curved moiré patterns can also be perfectly reproduced by the product $\boldsymbol{\varepsilon}_{DS} \cdot \boldsymbol{\varepsilon}_{MS}$ under the assumption of MSs with a slight curvature smaller than $\sim\frac{1}{100\,\mu m}$ (Supplementary Note 5). The line profiles thus obtained reveal an astonishing consistency between experiments and simulations, where the amplitude contrast of variations in optical conductivity resolved by our nanoimaging decays with decreasing periodicity (Fig. 3c; see also Supplementary Information Fig. 1). This consistency further confirms the validity of our interpretation. Furthermore, the variations of the orientation and curvature of the MSs offer a unique opportunity to realize a diverse range of electronic moiré textures with different spatial configurations (Extended Data Fig. 8).

In Fig. 3d, another example of a curved moiré pattern is presented. The near-field line profile (Fig. 3f) demonstrates clear contrast between peaks and valleys of optical conductivity in the moiré pattern regions. On the other hand, regions without a clear moiré pattern reveal optical conductivity approximately equal to the average of that of the moiré fringes. Note that the borders between moiré and non-moiré regions coincide with the twin boundaries of the LAO substrate (red dashed lines in Fig. 3d–f). In Fig. 3e, the topographic variation up to 10 nm in height originates from the LAO substrate twin structures[28,29] (Extended Data Fig. 2a and Supplementary Note 1). No visible moiré-like topographic modulation can be seen. Here we give a phenomenological interpretation: the miscut steps in LAO possess markedly different periodicities, orientations and even curvatures on either side of the underlying
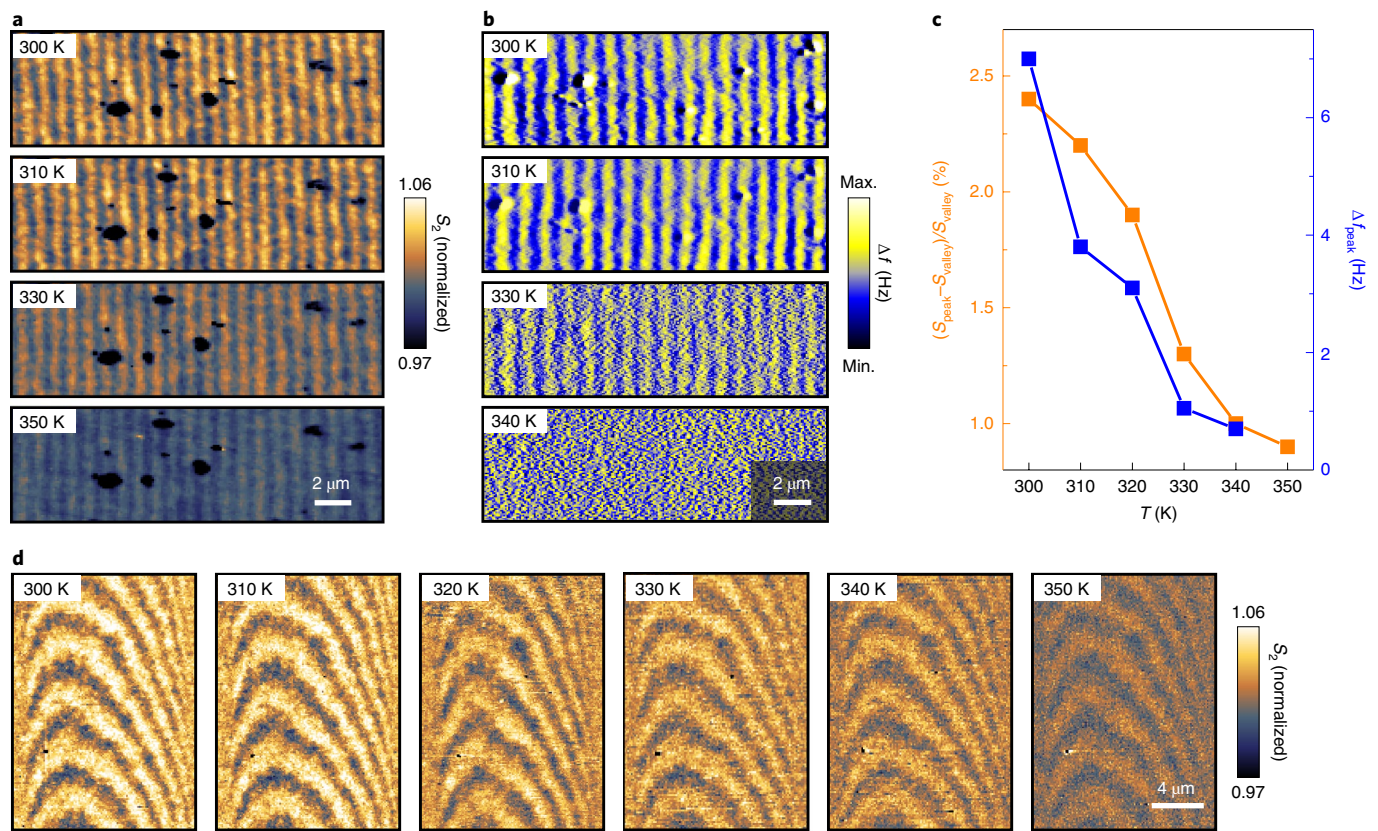
Fig. 4 | Temperature-dependent evolution of electronic and magnetic moiré patterns. a,b, Near-field and MFM images, respectively, of a moiré pattern measured at elevated temperatures. **c**, Temperature-dependent near-field contrast $(S_{peak} - S_{valley})/S_{valley}$ and MFM peak-frequency shift Δf_{peak} extracted from images in **a** and **b**, respectively. **d**, Near-field images of the curved moiré pattern obtained at different temperatures. All of the near-field images are normalized to dark fringes to demonstrate the relative contrast fading with increasing temperature.

LAO twin boundaries (Extended Data Fig. 9). As simulated in Fig. 3g (detailed in Extended Data Fig. 8c), to the right of the LAO twin boundary, the small twist angle between DS and MS leads to a relatively large moiré pattern periodicity that can be observed under near-field imaging. To the left of the LAO twin boundary, the large twist angle is expected to produce a moiré pattern with a much smaller periodicity, of the same order as the DSs or MSs. As demonstrated in Fig. 3c and Supplementary Information Fig. 1, smaller periodicity yields a smaller infrared near-field intensity contrast. The spatial features are therefore indistinguishable under the near-field mapping due to minimal conductivity variation between the electronic domains. This is supported experimentally by the average signal level detected for the non-moiré regions in Fig. 3f.

Temperature-dependent s-SNOM and magnetic force microscopy (MFM) measurements provide further insight into the interdependence between electronic and magnetic moiré textures in strained LSMO. As a hallmark feature of the colossal magnetoresistive manganites, the microscopic mechanism of electrical conductivity in LSMO is intimately tied to the onset of long-range ferromagnetic order[9], and here we report moiré-like modulations of that dependence borne out and resolved at the mesoscale. Clear fringes in moiré conductivity are observed with a periodicity of ~1.05 μm at room temperature, as shown in the near-field images of Fig. 4a. Figure 4b shows the MFM images acquired in roughly the same region, where clear frequency-shift contrast with the periodicity of ~1.13 μm is observed at 300 K, demonstrating the moiré modulations of local ferromagnetism. Increasing the temperature prompts a decrease in both the nano-infrared contrast and magnetic response (Fig. 4c). This latter observation implies a positive

correlation between the conductivity and the local ferromagnetic moment, consistent with the established phase diagram of LSMO[15]. The observed magnetic moiré fringes disappear at the ferromagnetic–paramagnetic transition temperature of 340 K (Fig. 4b and Supplementary Information Fig. 3), while the electronic counterpart persists with a greatly reduced nano-infrared contrast up to all measurable temperatures (Fig. 4a). This may suggest that two distinguishable sets of ferromagnetic metal states with different strain environments transfer to two paramagnetic metal states at T_C. Above T_C no magnetization persists, but detectable near-field contrast is still present due to the local strain modulation. The temperature evolution of a curved moiré pattern is also shown in Fig. 4d. It is evident that the near-field optical contrast of the moiré pattern decays substantially at higher temperatures. Such an observation further validates that the electronic and magnetic properties of the moiré patterns are closely related to the T_C of LSMO/LAO thin films.

Finally, we wish to point out that the individual DS and MS stripes are barely observable under s-SNOM, but their combined electronic effects nevertheless manifest clearly through the moiré pattern formation (Extended Data Fig. 10). This 'magnified' electronic response may be potentially useful for identifying 'hidden' textures of strain, electronic or magnetic distribution in CTMO thin films, where individual traits are difficult to identify separately.

In summary, our work reports the ordered electronic and magnetic mesoscale patterns in LSMO, demonstrating the feasibility of producing and visualizing surface moiré patterns that yield optical contrast. In the large family of CTMO, there are many oxide systems that host substantial nonlinear strain coupling, for example those

with a cubic or pseudocubic crystal structure, and a relatively large Jahn–Teller effect[24]. Our novel approach thus provides a strategy for manipulating complex electronic orders in strongly correlated quantum materials such as $NdNiO_3$[22,30] or $SrTiO_3$[31], where long-wavelength electronic and lattice modulations similar to those exploited here have been reported. Beyond the long-wavelength moiré patterns, it is also interesting to explore similar effects at shorter length scales. Materials with competing phases or proximate to a quantum phase transition can be tested with high priorities (for example the interplay between the stripe and superconducting phases in high-T_C cuprates is affected by strain).

Online content

Any methods, additional references, Nature Research reporting summaries, source data, extended data, supplementary information, acknowledgements, peer review information; details of author contributions and competing interests; and statements of data and code availability are available at https://doi.org/10.1038/s41567-020-0865-1.

References

1. Cao, Y. et al. Unconventional superconductivity in magic-angle graphene superlattices. *Nature* **556**, 43–50 (2018).
2. Cao, Y. et al. Correlated insulator behaviour at half-filling in magic-angle graphene superlattices. *Nature* **556**, 80–84 (2018).
3. Jin, C. et al. Observation of moiré excitons in WSe_2/WS_2 heterostructure superlattices. *Nature* **567**, 76–80 (2019).
4. Tran, K. et al. Evidence for moiré excitons in van der Waals heterostructures. *Nature* **567**, 71–75 (2019).
5. Seyler, K. L. et al. Signatures of moiré-trapped valley excitons in $MoSe_2/WSe_2$ heterobilayers. *Nature* **567**, 66–70 (2019).
6. Sunku, S. S. et al. Photonic crystals for nano-light in moiré graphene superlattices. *Science* **362**, 1153–1156 (2018).
7. Geim, A. K. & Grigorieva, I. V. Van der Waals heterostructures. *Nature* **499**, 419–425 (2013).
8. Dagotto, E. Complexity in strongly correlated electronic systems. *Science* **309**, 257–262 (2005).
9. Dagotto, E., Hotta, T. & Moreo, A. Colossal magnetoresistant materials: the key role of phase separation. *Phys. Rep.* **344**, https://doi.org/10.1016/S0370-1573(00)00121-6 (2001).
10. Liu, M., Sternbach, A. J. & Basov, D. N. Nanoscale electrodynamics of strongly correlated quantum materials. *Rep. Prog. Phys.* **80**, 014501 (2017).
11. Lu, C. J., Wang, Z. L., Kwon, C. & Jia, Q. X. Microstructure of epitaxial $La_{0.7}Ca_{0.3}MnO_3$ thin films grown on $LaAlO_3$ and $SrTiO_3$. *J. Appl. Phys.* **88**, 4032 (2000).
12. Zhang, L., Israel, C., Biswas, A., Greene, R. L. & de Lozanne, A. Direct observation of percolation in a manganite thin film. *Science* **298**, 805–807 (2002).
13. Wu, W. et al. Magnetic imaging of a supercooling glass transition in a weakly disordered ferromagnet. *Nat. Mater.* **5**, 881–886 (2006).
14. McLeod, A. S. et al. Multi-messenger nanoprobes of hidden magnetism in a strained manganite. *Nat. Mater.* https://doi.org/10.1038/s41563-019-0533-y (2019).
15. Urushibara, A. et al. Insulator-metal transition and giant magnetoresistance in $La_{1-x}Sr_xMnO_3$. *Phys. Rev. B* **51**, 14103–14109 (1995).
16. Angeloni, M. et al. Suppression of the metal-insulator transition temperature in thin $La_{0.7}Sr_{0.3}MnO_3$ films. *J. Appl. Phys.* **96**, 6387–6392 (2004).
17. Lebedev, O. I., Van Tendeloo, G., Amelinckx, S., Razavi, F. & Habermeier, H.-U. Periodic microtwinning as a possible mechanism for the accommodation of the epitaxial film-substrate mismatch in the $La_{1-x}Sr_xMnO_3/SrTiO_3$ system. *Philos. Mag. A* **81**, 797–824 (2001).
18. Farag, N., Bobeth, M., Pompe, W., Romanov, A. E. & Speck, J. S. Modeling of twinning in epitaxial (001)-oriented $La_{0.67}Sr_{0.33}MnO_3$ thin films. *J. Appl. Phys.* **97**, 113516 (2005).
19. Sandiumenge, F. et al. Competing misfit relaxation mechanisms in epitaxial correlated oxides. *Phys. Rev. Lett.* **110**, 107206 (2013).
20. Santiso, J. et al. Thickness evolution of the twin structure and shear strain in LSMO films. *CrystEngComm* **15**, 3908 (2013).
21. Balcells, L. et al. Enhanced conduction and ferromagnetic order at (100)-type twin walls in $La_{0.7}Sr_{0.3}MnO_3$. *Phys. Rev. B* **92**, 075111 (2015).
22. Mattoni, G. et al. Striped nanoscale phase separation at the metal–insulator transition of heteroepitaxial nickelates. *Nat. Commun.* **7**, 13141 (2016).
23. Hillenbrand, R., Knoll, B. & Keilmann, F. Pure optical contrast in scattering-type scanning near-field microscopy. *J. Microsc.* **202**, 77–83 (2001).
24. O'Callahan, B. T. et al. Inhomogeneity of the ultrafast insulator-to-metal transition dynamics of VO_2. *Nat. Commun.* **6**, 6849 (2015).
25. Millis, A. J., Darling, T. & Migliori, A. Quantifying strain dependence in "colossal" magnetoresistance manganites. *J. Appl. Phys.* **83**, 1588–1591 (1998).
26. Millis, A. J. Lattice effects in magnetoresistive manganese perovskites. *Nature* **392**, 147–150 (1998).
27. Tsui, F., Smoak, M. C., Nath, T. K. & Eom, C. B. Strain-dependent magnetic phase diagram of epitaxial $La_{0.67}Sr_{0.33}MnO_3$ thin films. *Appl. Phys. Lett.* **76**, 2421–2423 (2000).
28. Bueble, S., Knorr, K., Brecht, E. & Schmahl, W. W. Influence of the ferroelastic twin domain structure on the {100} surface morphology of $LaAlO_3$ HTSC substrates. *Surf. Sci.* **400**, 345–355 (1998).
29. Geddo Lehmann, A. et al. Effect of the substrate ferroelastic transition on epitaxial $La_{0.7}Sr_{0.3}MnO_3$ films grown on $LaAlO_3$. *Eur. Phys. J. B* **55**, 337–345 (2007).
30. Caviglia, A. D. et al. Ultrafast strain engineering in complex oxide heterostructures. *Phys. Rev. Lett.* **108**, 136801 (2012).
31. Frenkel, Y. et al. Imaging and tuning polarity at $SrTiO_3$ domain walls. *Nat. Mater.* **16**, 1203–1208 (2017).

Methods

Sample fabrication and characterization. LSMO thin films of varying thicknesses were grown on the LAO(001) substrates at 700 °C via pulsed laser deposition. A KrF excimer laser was used with an energy density of 5.5 J cm^{-3} and a 3-Hz repetition rate. The O_2 pressure was maintained at 40 Pa during growth. The as-grown films were then in situ annealed for 0.5 h under the deposition conditions, followed by ex situ annealing in a tube furnace at 780 °C in flowing O_2. The lattice parameters and crystalline quality of the films were characterized by XRD (Panalytical X'Pert PRO MRD) and cross-sectional TEM at room temperature, with typical results for the 20-nm sample shown in Extended Data Fig. 1. Our films are found to be of good crystalline and epitaxial quality. The relatively large full-width at half-maximum of the rocking curve of the LSMO 002 reflection indicates the appearance of bending or twinning of the 002 crystal plane, which is consistent with the lattice strain effect proposed above for the moiré pattern. The magnetic properties were analysed using a Quantum Design SQUID-VSM system. The electrical transport properties were measured using the four-probe method in a Quantum Design PPMS system.

Infrared s-SNOM. Measurements were conducted with two different s-SNOM apparatuses, yielding nearly identical results. Monochromatic light of wavelength ~11 μm (~10.7 μm for the other s-SNOM) was focused onto an AFM probe with tip apex radius ~25 nm. The AFM probe was operated in tapping mode with oscillation frequency $\Omega \sim 250$ kHz and amplitude $A \sim 50$ nm (~80 nm for the other s-SNOM). Backscattered light from the tip–sample ensemble interfered with the reference light to yield phase-resolved infrared near-field detection. Lock-in demodulation at higher harmonics of Ω could largely eliminate undesired background and preserve the genuine local near-field interaction emanating from the confined area below the tip apex. In our measurements, the amplitudes of the nano-infrared signal demodulated at the second/third/fourth harmonic of the tip tapping frequency ($S_2/S_3/S_4$) showed essentially identical results, and the S_2 signal was finally presented for better signal-noise ratio.

MFM. MFM measurements were performed under zero magnetic field with a home-made MFM. Using electron-beam deposition, the tip was coated with a trilayer film of 5 nm Ti, 50 nm Co and 5 nm Au, which was subsequently magnetized with a permanent magnet along the tip axis. The MFM images were obtained in the frequency mode, in which the frequency shift Δf ($\Delta f = f - f_0$) was 'tracked' by a commercial phase-locked loop. A negative frequency shift indicates an attractive tip−sample interaction ($\Delta f < 0$), while a positive frequency shift indicates a repulsive tip−sample interaction ($\Delta f > 0$).

OC-SEM. The rhombohedral domains in the LSMO/LAO samples were characterized using OC-SEM imaging, with misorientation between different domains represented by different contrast levels. The measurements were conducted in a field emission scanning electron microscope (ZEISS GeminiSEM 500) using the in-lens mode. The typical values of the acceleration voltage, objective aperture size and working distance were 1 kV, 120 μm and 5 mm, respectively.

Data availability
The data represented in Figs. 1–4 are available as Source Data 1–4. All other data that support the plots within this paper and other findings of this study are available from the corresponding author upon reasonable request.

Author contributions
M.L., C.Z. and D.N.B. designed and supervised the work. X.C. and X.F. performed the s-SNOM measurements with assistance from Z.N., S.X., D.W. and H.Z.; L.L., N.Z. and H.X. fabricated the samples and performed the XRD, magnetic and transport characterizations; T.G. and Q.L. performed the MFM measurements; X.C., L.L., X.F., D.N.B., M.L. and C.Z. analysed the data and wrote the manuscript. A.S.M., A.J.M. and Z.L. contributed to data interpretation and presentation. All authors contributed to the scientific discussion and manuscript revisions.

Competing interests
The authors declare no competing interests.

Additional information
Extended data is available for this paper at https://doi.org/10.1038/s41567-020-0865-1.

Supplementary information is available for this paper at https://doi.org/10.1038/s41567-020-0865-1.

Correspondence and requests for materials should be addressed to L.L., D.N.B., M.L. or C.Z.

Peer review information *Nature Physics* thanks Maria Calderon and the other, anonymous, reviewer(s) for their contribution to the peer review of this work.

**Reprints and permissions information** is available at www.nature.com/reprints.
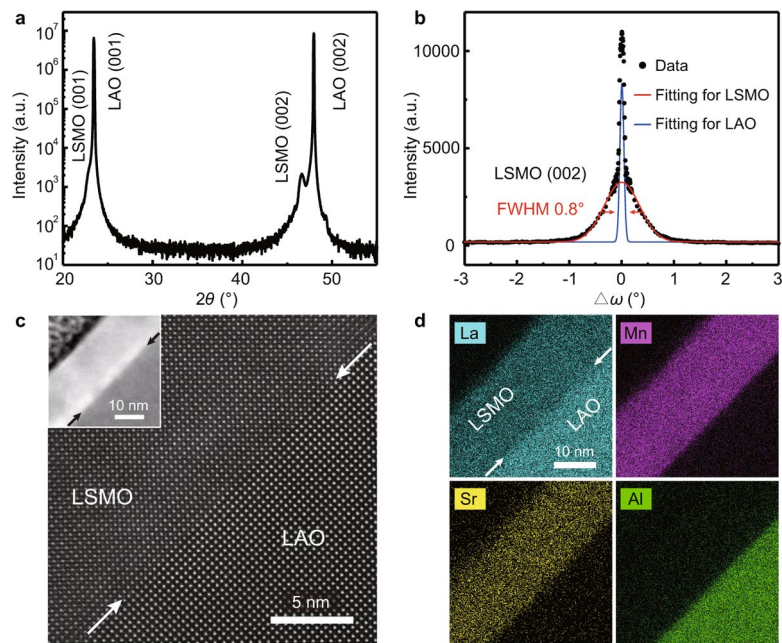
Extended Data Fig. 1 | Structure characterizations of LSMO thin film grown on LAO substrate. a, X-ray diffraction spectrum of a 20-nm-thick LSMO/LAO film. The LSMO thin films are clearly single-crystalline and coherently epitaxial on the LAO (001) substrates. The LSMO film's out-of-plane lattice constant as determined by the XRD peak is c=3.90 Å, which slightly exceeds the bulk value of 3.87 Å. The out-of-plane expansion, or tensile strain, proceeds from the compressive in-plane strain from the LAO substrates (pseudo-cubic structure with a lattice constant of 3.79 Å). **b**, The rocking curve of the (002) reflection of LSMO thin film. The data can be well fitted with the sum of two Gaussian peaks, one (red) originates from LSMO film and the other (blue) is due to a contribution of the substrate. **c**, Atomically resolved cross-sectional TEM image of a 20-nm LSMO/LAO film, showing that the film has good epitaxial quality with a sharp interface structure. The interface between LSMO and LAO is indicated by white arrows. Inset: low magnification TEM image. **d**, Energy dispersive spectroscopy (EDS) elemental mapping images across the interface.
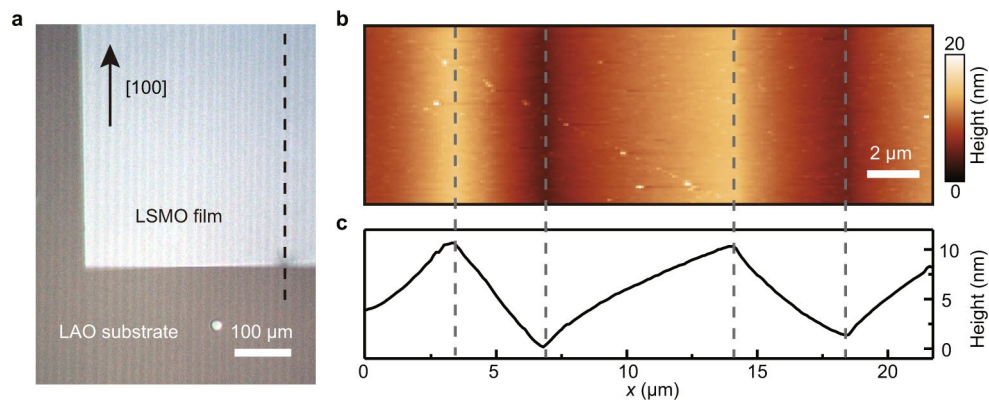
Extended Data Fig. 2 | Twin structures in LAO substrates. a, Optical image of a LAO substrate with the surface partially covered by LSMO thin films. Twin structure fringes of the LAO substrate are visible across the LSMO film edge, lying parallel to the guiding black dashed line. **b,c**, AFM image and corresponding height profile of the twin structures in the LAO substrate.
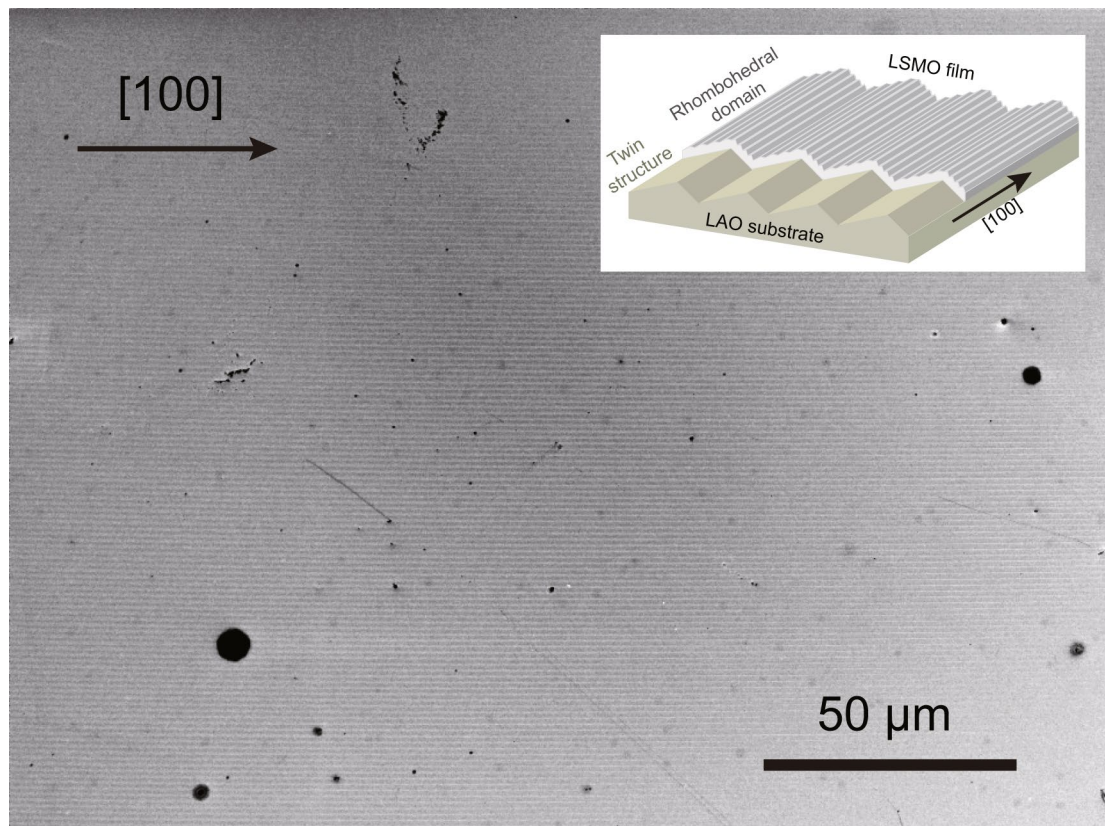
Extended Data Fig. 3 | Rhombohedral domains in the LSMO films on LAO substrates. Large-scale OC-SEM image of a LSMO thin film showing surface rhombohedral domains. The inset demonstrates that the direction of rhombohedral domains in LSMO is identical to that of the LAO twins, running along the LAO [100] direction.
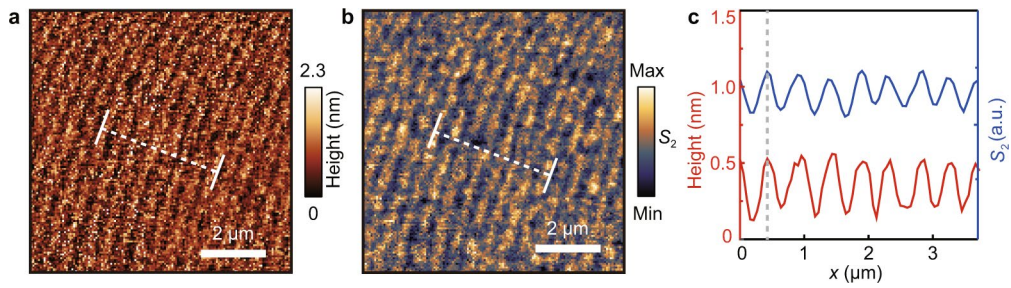
Extended Data Fig. 4 | Miscut stripes (MS)-induced electronic pattern in LSMO. a, AFM image of a LSMO/LAO sample showing surface steps due to miscuts on the LAO substrate. **b**, Corresponding near-field image obtained simultaneously with the AFM image in a, showing spatially alternating values of IR near-field signal. **c**, Line profiles along the dashed lines in a and b show that near-field signal is positively correlated to the topography of miscut steps.
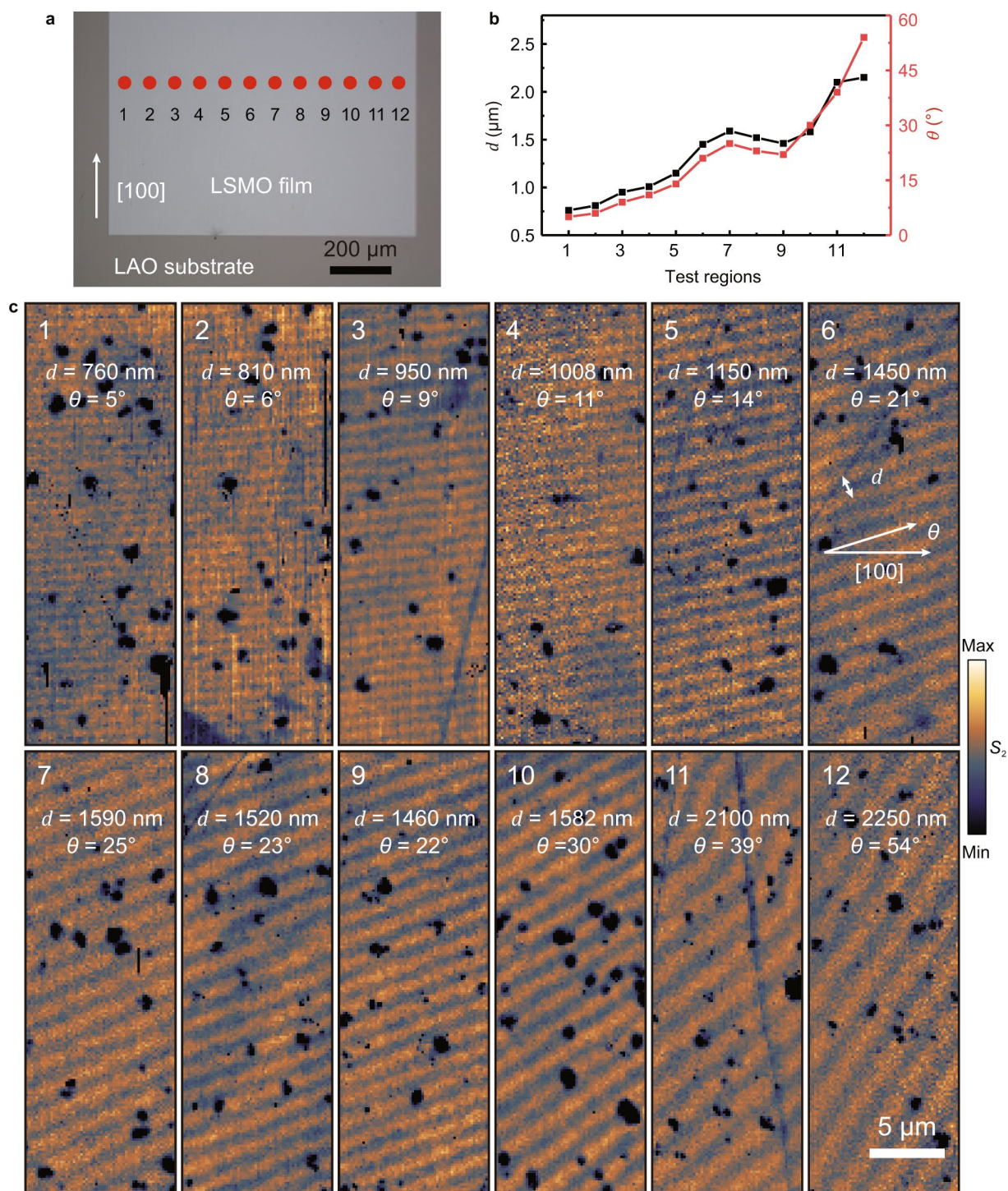
Extended Data Fig. 5 | Variation of electronic moiré patterns across the LSMO film. a, Optical image of a LSMO thin film on LAO substrate. **b**, The concurrent variations of periodicity d and angle θ for moiré patterns obtained from different regions (numbered and marked in a by red circles). **c**, IR near-field images taken from different regions (1 to 12) marked in **a**.
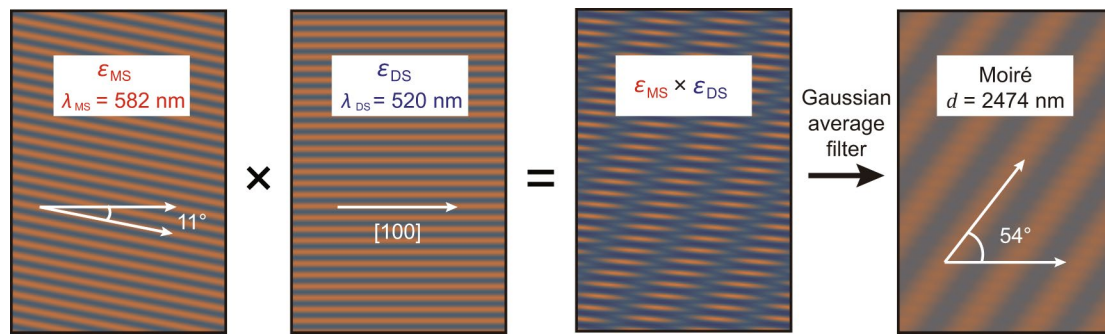
Extended Data Fig. 6 | Simulation of moiré pattern. The moiré pattern can be simulated by multiplying two periodic striped patterns representing DS and MS and then imposing a Gaussian average filter with radius ~100 nm. The simulation details are described in Supplementary Note 4.
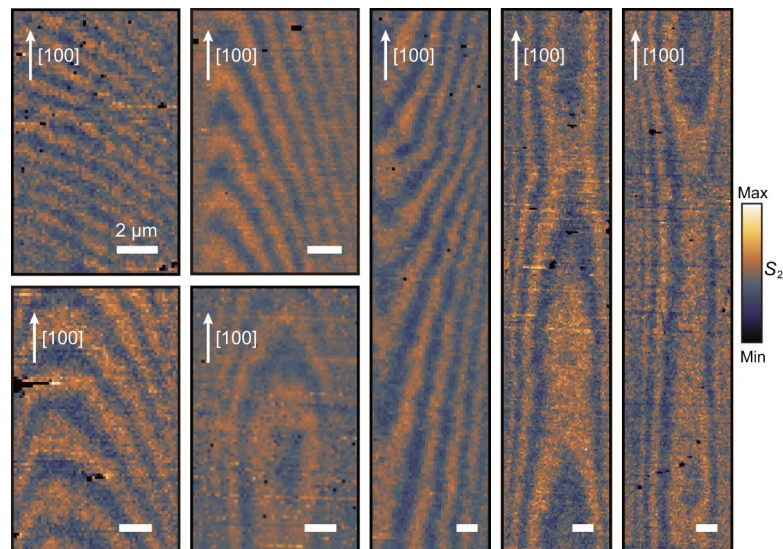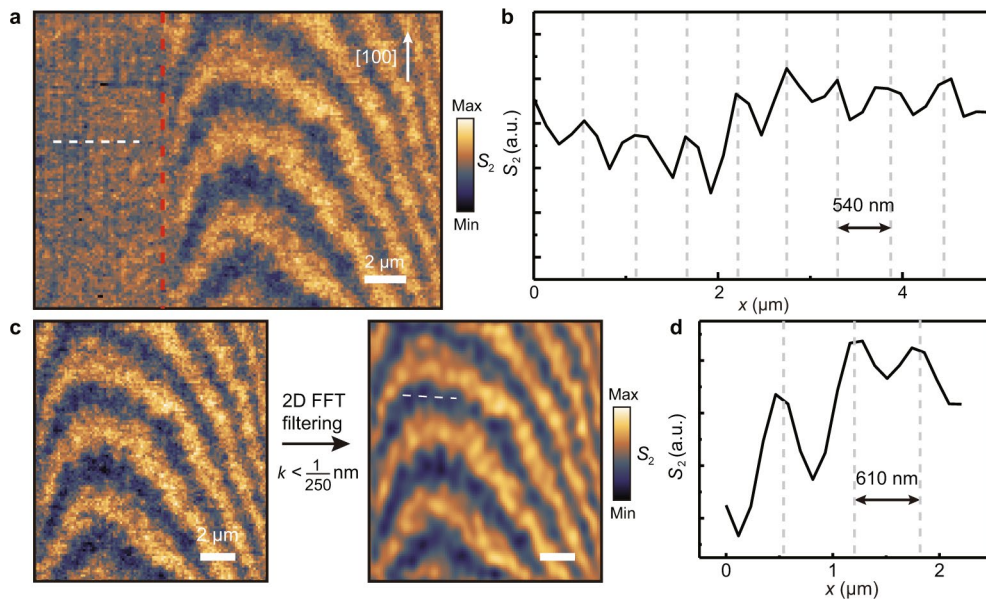
Extended Data Fig. 7 | A display of near-field images of a variety of moiré patterns. Different manifestations of moiré patterns observed across the film with vastly distinctive periodicities.
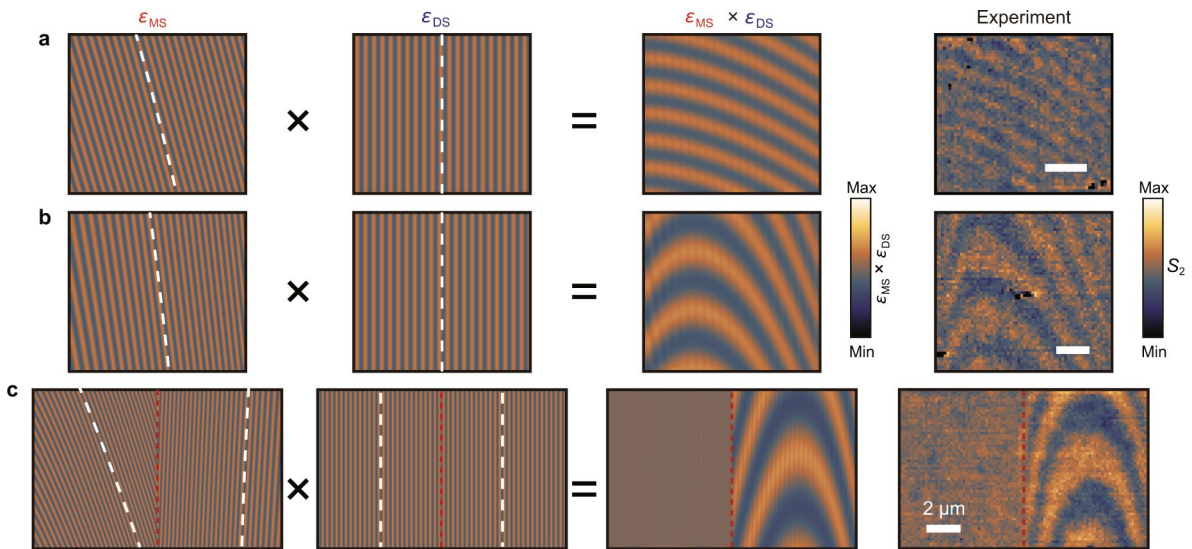
Extended Data Fig. 8 | Simulations of the curved moiré patterns. a–c, Typical manifestations of curved moiré patterns (right panel) and how they are simulated (left panel). White dashed lines indicate the directions of MS and DS. Curved MS was achieved via adding a spatially varying phase $\phi(y)$ into ε_{MS} (the MS-induced strain field) during the simulation (see Supplementary Note 4 and 5). Red dashed lines indicate the LAO twin boundaries.
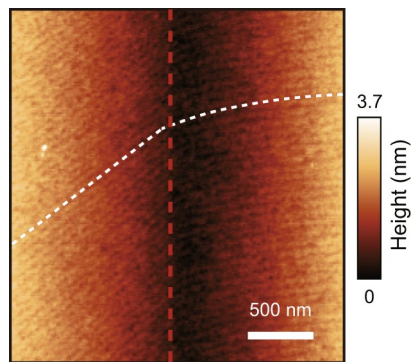
Extended Data Fig. 9 | Diversity of miscut steps in the LAO substrates. AFM image of a LAO substrate revealing that the miscut steps change their orientations (traced by the white dashed lines) and periodicities across the twin boundary of LAO (indicated by the red dashed line). This is common in commercially available LAO substrates.

Extended Data Fig. 10 | Evidence of the fine structures. a, Near-field image taken across the LAO twin boundary (indicated by the red dashed line). On the non-moiré region (left), DS-induced electronic pattern can be faintly identified in the nano-IR contrast. **b**, Line profile of the white dashed line in a. The period is ~540 nm, consistent with the OC-SEM image of DS. **c**, Near-field image taken on the moiré region in a and filtered with a Fourier filter for $k < \frac{1}{250\,nm}$. Fine structures of the electronic pattern corresponding to MS (or DS) can be observed. **d**, Line profile across the fine structure. The period is ~610 nm, qualitatively consistent with the typical MS (or DS) periodicity.